Oxidation and high-temperature radiative properties of the Kanthal Super ER intermetallic alloy

J. Colas, L. Charpentier, D. Chen, E. Bêche, Jérôme Esvan, D. de Sousa de Sousa Meneses, F. Mercier, M. Pons, Marianne J.H. Balat-Pichelin

Journal Pre-proof

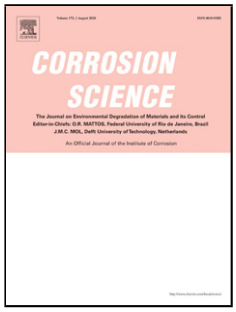

Oxidation and high-temperature radiative properties of the Kanthal Super ER intermetallic alloy

J. Colas, L. Charpentier, D. Chen, E. Bêche, J. Esvan, D. De Sousa Meneses, F. Mercier, M. Pons, M. Balat-Pichelin

PII: S0010-938X(21)00367-X

DOI: https://doi.org/10.1016/j.corsci.2021.109601

Reference: CS 109601

To appear in: *Corrosion Science*

Received Date: 8 January 2021

Revised Date: 29 April 2021

Accepted Date: 30 May 2021

Please cite this article as: Colas J, Charpentier L, Chen D, Bêche E, Esvan J, Meneses DDS, Mercier F, Pons M, Balat-Pichelin M, Oxidation and high-temperature radiative properties of the Kanthal Super ER intermetallic alloy, *Corrosion Science* (2021), doi: https://doi.org/10.1016/j.corsci.2021.109601

Oxidation and high-temperature radiative properties of the Kanthal Super ER intermetallic alloy

J. Colas[1], L. Charpentier[1,*], D. Chen[2], E. Bêche[1], J. Esvan[3], D. De Sousa Meneses[4], F. Mercier[2], M. Pons[2], M. Balat-Pichelin[1]

[1] PROMES-CNRS, 7 Rue du Four Solaire, F-66120 Font-Romeu Odeillo, France

[2] SIMaP-CNRS/Université Grenoble-Alpes/Grenoble INP, 1130 rue de la piscine, Domaine Universitaire, BP75, F-38402 Saint-Martin d'Hères, France

[3] CIRIMAT-CNRS, 4 Allée Emile Monso, F-31400 Toulouse, France

[4] CEMHTI-CNRS, 1D avenue de la Recherche Scientifique, F-45071 Orléans, France

Highlights

- The potential of the Kanthal Super ER (KSER) for solar applications is evaluated
- KSER is oxidized in muffle or solar furnaces at 1373, 1600, 1850 or 2100 K
- The oxidation in air in temperature follows semi-parabolic or subparabolic kinetics
- The radiative properties are not drastically affected by the oxidation

Abstract. The oxidation resistance of receivers is a critical point in the development of plants using solar tower technology. Intermetallics in Mo-Si-Al system present oxidation maximum temperature and creep resistance superior to the ones of the currently used Ni-based alloys. We followed here the oxidation resistance of such intermetallic exposed to different treatments in air: long-term oxidation (up to 700 h) at 1373 K, and for several cycles of 20 minutes in solar furnace. The normal spectral emissivity is measured up to 1640 K in air, and our main positive conclusion is this property is not degraded by the oxidation.

Keywords. A. Intermetallics ; C. Oxidation ; B. Thermal cycling ; B. XPS ; B. Raman spectroscopy ; B. SEM

1. Introduction

Among the various technologies used in the Concentrated Solar Power (CSP) plants, the systems concentrating the incoming solar flux on the surface of the receiver placed at the top of a central tower are the most promising ones. The receiver could reach working temperature above 1000 K, improving the fraction of the incoming solar power converted into heat, then into electricity. As an example, Segal *et al.* have calculated an optimal temperature of 1500 K

* Corresponding author, ludovic.charpentier@promes.cnrs.fr

using a heliostat field density of 37% [1]. As another example, Kribus *et al.* have simulated that the converted fraction can overpass 45% with a combined cycle (using firstly a Brayton cycle with a pressured gas as coolant, then a Rankine cycle with water steam) [2]. Nevertheless, although 1270 K is the temperature requested for the Brayton cycle, the gas issuing the current receivers cannot reach temperatures above 1020 K [3], due to the high-temperature limitations of the Ni-alloys used, especially its resistance towards oxidation. Figure 1 presents three figures of merit (built from the existing industrial datasheets and literature [4-20]) comparing the reported performances of Ni-based alloys (chromia and alumina formers) and of other alloys (Kanthal APMT, TZM, tungsten….), ceramics (SiC/SiC), MAX phases (Ti_3SiC_2) and disilicide ($MoSi_2$) compounds. The intermetallic compounds $MoSi_2$ presents an important oxidation maximum temperature in dry air, with a creep resistance higher than the one of Inconel, nevertheless this material is fragile and its fracture toughness would have to be improved. Maruyama *et al.* [21] have investigated the influence of the incorporation of aluminum on the oxidation in air of $Mo(Si_{1-x}Al_x)_2$ materials with $x = 0$ ($MoSi_2$), 0.14 and 0.28. They observed silica formed at 1823 K for the $MoSi_2$ samples whereas alumina was the oxide formed when x was 0.14 and 0.28. At 2048 K, $MoSi_2$ oxidized to form molten silica. The alumina formed at 2048 K dissolves into the molten silica. At both temperatures the oxidation rate increases when the x ratio of aluminum increases, but the presence of aluminum reduces the cracking and the spallation of the oxide layers during cooling compared to the ones formed on pure $MoSi_2$.

Kanthal Super ER is an alloy supplied by Sandvik AB (Sweden) with a main phase $Mo(Si,Al)_2$ that has shown promising oxidation resistance at 1270 K [22]. Oxidation performed at 1770 K in synthetic air has shown the formation of a protective oxide scale after up to 168 h oxidation time [23]. In a previous work [24], the oxidation kinetics and room temperature optical properties of the currently used Inconel 625 have been compared to those of the alternative alloys FeCrAlloy and Kanthal Super ER (KSER) and this latest one supported 48 h oxidation at 1373 K in air inside a muffle furnace with the weakest weight change.

In this work, we continued the investigation on the performance of the KSER alloy using the unique solar facilities of the PROMES-CNRS laboratory to perform high temperature oxidation with thermal shocks similar to the ones encountered in solar power plants. These results were compared with long-time oxidations performed in two different muffle furnaces, up to 700 h. This comparison between oxidation in solar furnaces with thermal shocks and

longer-term oxidation has never been previously studied as far as we know. Moreover, the high temperature normal spectral emissivity is measured using the set-up developed at the CEMHTI-CNRS laboratory. Such an exploration of high-temperature radiative properties of KSER has never been performed before to our knowledge. Both oxidation resistances under concentrated solar fluxes and high temperature radiative properties are to explore to define the potential interest of this intermetallic alloys in CSP applications.

2. Material and methods

Three phases compose the Kanthal Super ER alloy: hexagonal $Mo(Si,Al)_2$ (80 vol.%), $Mo_5(Si,Al)_3$ (6 vol.%) and Al_2O_3 (13 vol.%) [25]. An 18 mm diameter cylinder was cut into several disks whose thicknesses range from 2 to 3 mm. These disks were polished in order to reach a quadratic surface roughness between 0.5 and 0.8 µm, with the procedure previously described [24].

Various structural analyses are achieved to investigate the changes due to oxidation. XRD is carried out with a PANanalytical X'Pert Pro diffractometer operating at 40 kV and 20 mA (Kα radiation of Cu, $\lambda = 0.15418$ nm) and in the 2θ range of 20-100°. Surface and cross-section SEM images are obtained with a Hitachi S-4500 apparatus, using the secondary electrons (SE), with a detector sufficiently close to the sample to capture part of the backscattered electrons. The EDS analyses were performed on this SEM with an acceleration voltage of 15 kV. The micro-Raman analyses are performed with a Horiba Jobin Yvon spectrometer (LabRAM HR evolution), using a 532 nm green laser.

XPS analysis is performed using a KAlpha ThermoScientific device at CIRIMAT-CNRS. The photoelectron emission spectra are recorded using Al-Kα radiation (hν=1486.6 eV) from a monochromatised source. The analysed area is approximately 0.15 mm^2. The pass energy of window scan is fixed at 20 eV (single spectrum of element) and 150 eV (survey). The spectrometer energy calibration is made using the Au $4f_{7/2}$ (83.9 ± 0.1 eV) and Cu $2p_{3/2}$ (932.8 ± 0.1 eV) photoelectron lines. XPS spectra are recorded in direct N(Ec). The atomic concentrations were determined with an accuracy of 8 % from photoelectron peak areas using the atomic sensitivity factors reported by Scofield [26], taking into account the transmission function of the analyser. This function was calculated at different pass energies from Ag 3d and Ag MNN peaks collected for a silver reference sample. The binding energy scale is established by referencing the C 1s value of adventitious carbon (284.8 eV [27]). The photoelectron peaks were analysed by Gaussian/Lorentzian (G/L=50) peak fitting. The

background signal was removed using the Shirley method [28]. According to our observations on degradation surface by ions [29], the ionic sputtering of the films surfaces was made by Ar^+ ion beam accelerated under 1 keV. The ion flux was fixed at about 1.5 µA cm^{-2} for five seconds.

Long-term oxidations are performed inside two muffle furnaces in stagnant ambient air at 1373 K. The one located in PROMES-CNRS laboratory is used for oxidation during 24 to 48 h. The SIMaP-CNRS laboratory allows to process longer oxidation time, one KSER sample was oxidized during 700 h using one of their muffle furnaces. Samples are regularly extracted from the furnaces and weighted to determine the mass variation.

Oxidations are also performed using the solar reactor REHPTS (*REacteur Hautes Pression et Température Solaire* – High Pressure and Temperature Solar Reactor) whose technical features can be found in our previous works [30, 31]. Inside this reactor, the samples are placed in open and stagnant ambient air at P = 87 kPa and insolated on a face whose temperature is measured using a solar-blind optical monochromatic pyrometer at λ = 5 µm. The sample is positioned so that the temperature is homogeneous on a 10 mm diameter area and is oxidized during 5 or 6 cycles of 20 min. at 1600, 1850 and 2100 K, being weighted after each oxidation cycle. For both experimental set-up, the mass variations are divided by the surface exposed to air (the upper surface and the lateral one, the one for which the sample is placed on the sample holder being excluded) to be expressed in mg cm^{-2}.

High-temperature radiative properties are measured on the set-up developed by the CEMTHI-CNRS that was previously described [32]. A 500 W CO_2 laser (Coherent K500, λ = 10.6µm) heats the sample, while mirrors and a separator insure an equitable heating on both faces of the sample. Two Bruker infrared spectrometers, a VERTEX 80v and a VERTEX 70, were used to measure the radiance from 0.56 to 26 µm. A reference blackbody is placed on the same turntable holding the sample, so that the spectrometers can be continuously calibrated. The temperature of the sample is obtained using the ALVARAES algorithm [33], a method allowing the simultaneous determination of temperature and emissivity from *in situ* acquisition of reflectance and emission fluxes. The measurements are done on one non-oxidized sample and on one pre-oxidized sample (48h inside a muffle furnace at 1373 K in air) to highlight the effects of oxidation during *in situ* growing and the impact that a previously grown oxide layer could bring.

The integration of the measured normal spectral emissivities using eq. (1) and (2) gives the approximate values (where λ_0 and λ_N are the minimum and maximum limits of the wavelengths measurement interval, N the number of divisions in this interval) of the solar absorptivity and total emissivity of the material according to the temperature T. In equation (1), $I(\lambda)$ is the incoming solar irradiance that can be found online. We used the Reference Air Mass 1.5 Spectra (tabulated from 0.28 to 4 µm) from the National Renewable Energy Laboratory [34]. $E_{bb}(\lambda, T)$ in equation (2) is the blackbody emittance at T and is calculated using the Planck's law.

$$\alpha(T) = \frac{\int_0^{+\infty} \varepsilon(\lambda,T).I(\lambda).d\lambda}{\int_0^{+\infty} I(\lambda).d\lambda} \approx \frac{\sum_0^{N-1} \varepsilon(\lambda_n,T).I(\lambda_n).(\lambda_{n+1}-\lambda_n)}{\sum_0^{N-1} I(\lambda_n).(\lambda_{n+1}-\lambda_n)} \quad (1)$$

$$\varepsilon(T) = \frac{\int_0^{+\infty} \varepsilon(\lambda,T).E_{bb}(\lambda,T).d\lambda}{\int_0^{+\infty} E_{bb}(\lambda,T).d\lambda} \approx \frac{\sum_0^{N-1} \varepsilon(\lambda_n,T).E_{bb}(\lambda_n,T).(\lambda_{n+1}-\lambda_n)}{\sum_0^{N-1} E_{bb}(\lambda_n,T).(\lambda_{n+1}-\lambda_n)} \quad (2)$$

3. Results

3.1. Oxidation kinetics

Figure 2 shows the mass variations of the KSER samples oxidized in the two muffle furnaces at 1373 K. Figure 2.b evidences the reproducibility of the 4 experiments as deviations are included in the error bars (due to the balance accuracy). The 700 h-oxidation test enables to determine the power law of the oxidation kinetics, with an exponent close to 0.5 in agreement with previous reported works on oxidation of KSER [25, 35]. However, a closer observation of figure 2.b indicates an under-estimation of the fitting curve for short oxidation time and an over-estimation of mass gain for long oxidation time. Therefore, a time dependence analysis of the exponent was performed as proposed by Naumenko *et al.* [36]. It reveals that the exponent varies from 0.79 for oxidation times below 48 h while it reaches a value of 0.42 above 48 h.

Figure 3 gives the mass variation of the three samples oxidized inside the REHPTS solar facility. A nearly semi-parabolic law with an exponent close to 0.6 fits the variations at 1600 K. At higher temperature, the fitting gives lower exponent values, closer to 0.3.

3.2. Characterizations

Figure 4 presents the XRD patterns of the samples oxidized inside the muffle furnaces (a) and REHPTS facility (b). We observe on every oxidized sample the appearance of the tetragonal Mo_5Si_3 phase whose peaks are identified using the ICDD file 89-5119. This phase is particularly present for the sample oxidized in the muffle furnace during 700 h. The amount of rhombohedral alumina (ICDD 73-6870) looks higher at the surface of the oxidized samples than the one found in the unoxidized sample corresponding to the initial amount of alumina, particularly for the ones oxidized inside REHPTS at higher temperature. The peaks of the MoSiAl hexagonal phase (ICDD 74-6555), present in the unoxidized sample, decrease when the oxidation temperature and time increase.

The micro-Raman analyses (figure 5) whose peaks are identified using literature data on the Raman analyses of silica [37, 38], alumina [39, 40], silicon and molybdenum disilicide [41] reveal the presence of various phases according to the operating conditions. An important peak is observed at 520 cm^{-1} after oxidation in the muffle furnace that corresponds to the one of polycrystalline silicon. The presence of alumina, silica and $MoSi_2$ can be observed after 36 h oxidation at 1373 K. The alumina peaks are higher and narrower on the samples oxidized inside REHPTS. Their proportion towards the other compounds increases with temperature and the alumina peaks are the only ones observable for the sample oxidized at 2100 K.

XPS results are presented in figure 6 and table 1. Figure 6 shows the O 1s photoelectron peaks for the unoxidized and oxidized KSER samples. The O 1s spectra were deconvoluted with 2 components, located at 532.5 ± 0.1 eV and 531.3 ± 0.2 eV respectively attributed to O-Si and to O-Al bonds. Table 1 resumes the atomic proportions of the components and of the main chemical bonds. Molybdenum is only present on the surface of the unoxidized sample, which is covered by a native oxide whose major phase is silica. Figure 6 and table 1 show that the major phase at the surface of the oxidized samples is alumina. Table 1 shows the alumina is nearly stoichiometric, with a ratio O-Al/Al-O between 1.3 and 1.6, whereas the O-Si/Si-O ratio decreases from 1.9 for the unoxidized sample to 0.8 for the samples oxidized in REHPTS at 1850 and 2100 K, far from the ratio of stoichiometric silica.

	Elements				Chemical bonds (Binding energy, eV)			
Sample treatment	O 1s	Si $2p_{1/2,3/2}$	Al $2p_{1/2,3/2}$	Mo $3d_{3/2,\ 5/2}$	O-Si (532.5 ± 0.1)	O-Al (531.3 ± 0.2)	Si-O (102.5 ± 0.5)	Al-O (74.7 ± 0.5)
Unoxidized	60	15.1	15.3	9.6	24.2	35.8	12.7	14.6
Muffle furnace, 36 h, 1373 K	59.3	7	33.7	/	15.5	43.8	7	33.7
REHPTS, 100 min, 1600 K	57.7	5.7	36.6	/	9.2	48.5	5.7	36.6
REHPTS, 120 min, 1850 K	55.9	4.6	39.5	/	3.9	52	4.6	39.5
REHPTS, 100 min, 2100 K	54.3	7.1	38.6	/	5.4	48.9	7.1	38.6

Table 1. Proportion (in atomic %) of the components and of the main chemical bonds (and associated energy) from XPS analyses.

Cross-section SEM images are achieved to estimate the oxide thickness. The samples oxidized in the muffle furnace (figure 7) present very thin oxide layers. The measured oxide thickness after 700 h oxidation time is 3.3 ± 0.4 µm. From the mass gain curve in figure 2, the calculated value of the oxide thickness is 3.5 µm, which is in agreement with the observed thickness by SEM. After 36 or 48 h oxidation time, the layer is too thin to determine its thickness with enough accuracy. The oxide layer is thicker for the samples oxidized at higher temperature inside REHPTS facility (figure 8 a-c). The thickness is 4.6 ± 0.5 µm for the sample oxidized at 1600 K during 100 min. and 8.2 ± 0.7 µm for the one oxidized at 1850 K during 120 min. These values are also in agreement with the thicknesses calculated from the mass gain (figure 3). The surface of the sample oxidized at 2100 K is less regular with the presence of oxide pockets inside cavities and the layer is too discontinuous to obtain a relevant oxide thickness. The EDS analyses performed on various spots of the cross section of the sample oxidized at 1850 K are presented in figure 8 d-f. We can observe between the oxide layer (only aluminum and oxygen elements, no silicon identified in figure 8 d) and the substrate (with Al, Mo, Si elements identified in figure 8 f) the presence of a 12.6 ± 1.9 µm thick intermediate clearer layer poorer in aluminum and silicon than the KSER substrate (figure 8 e). EDS performed on the sections presented in figure 8 a and c also did not reveal the presence of silicon in the oxide layer and that the intermediate clearer phase is poorer in aluminum.

Finally, figure 9 presents the SEM images of the surface of the oxidized samples compared with the unoxidized KSER sample. The samples oxidized in the muffle furnace for 24 or 48 h present dendrites of alumina on the oxide layer. The ones oxidized in REHPTS present a granular growth of the alumina, with a preferential growth at the grain boundaries. The higher the oxidation temperature is, the larger are the oxide grains.

3.3. High-temperature radiative properties

Figure 10 presents the evolution of the normal spectral emissivity for the as-received and pre-oxidized (in air at 1373 K during 48 h) samples. The measurements on the as-received samples (figure 10 a) show interference fringes and two emissivity peaks are growing *in situ*: one at 11.5 and one around 20 µm. These peaks are also present for the pre-oxidized sample (figure 10 b), and another peak is located at 8.9 µm for this sample.

Table 2 presents the estimated values of the solar absorptivity α, the total normal emissivity ε and of the α/ε ratio using eq. (1) and (2). Both solar absorptivity and total emissivity increase with the advancement of the oxidation, as this can be evidenced by the global increase of these values on the as-received sample when the temperature increases, and by higher values on the pre-oxidized sample at the same temperature level. It is noticeable that the solar absorptivity stays higher than the total emissivity for all of the samples, even after oxidation, despite the presence of emissivity peaks due to the oxide phases. As a comparison, in a recently published paper, the maximum α/ε ratio measured on Ni-based alloys was 1.10 at 1400 K [42].

As-received				**Pre-oxidized 48 h in air at 1373 K**			
T (K)	α	ε	α/ε	T (K)	α	ε	α/ε
560	0.49	0.37	1.32				
870	0.61	0.45	1.36				
1120	0.63	0.50	1.27				
1360	0.71	0.61	1.17	1370	0.76	0.65	1.16
1510	0.66	0.61	1.09	1430	0.80	0.67	1.21
1590	0.64	0.59	1.09	1540	0.76	0.68	1.13
1640	0.65	0.59	1.10	1600	0.73	0.67	1.08

Table 2. Estimated values of the solar absorptivity α, total emissivity ε and α/ε ratio from the high temperature normal spectral emissivity measurements, for as-received and pre-oxidized KSER samples.

4. Discussion

The oxidation of KSER in the presented conditions leads to the formation of an oxide layer made of distinct phases of alumina and silica. Both oxides are known to be protective and to favour a diffusion-control oxidation mode, which explains why the oxidation kinetics follow a power-law with an exponent below unity according to the mechanism previously described by Deal and Grove [43].

XRD reveals the presence of rhombohedral alumina on all the oxidized samples. Micro-Raman analyses reveal the presence of other phases (polycrystalline silicon, molybdenum disilicide and silica) on the samples oxidized inside the muffle furnace at 1373 K. At this temperature, aluminum seems to migrate from the substrate to form an alumina layer together with the formation of phases richer in silicon (and silica may form from partial oxidation of these phases). On the samples oxidized inside REHPTS, the higher the temperature is, the more alumina forms. This preponderance of alumina towards other phases is also deduced from the XPS analyses that also evidence that the O-Si/Si-O ratio decreases when the temperature increases, down to 0.8 at 1850 and 2100 K. This phenomenon can be related to previous works of Pierrat *et al.* [44] that identified gaseous SiO may be produced in composite materials oxidized in air at atmospheric pressure above 1800 K. Active oxidation of silicon could explain why silicon, silica and molybdenum disilicide are less present at higher temperature. SEM analysis of the cross-sections of the sample oxidized at 1850 K shows a 8.2 ± 0.7 µm alumina layer that covers an intermediate 12.6 ± 1.9 µm layer poorer in aluminum and silicon than the substrate. This layer could involve the Mo_5Si_3 phase identified in the XRD patterns, and its presence comforts the hypothesis that alumina was formed together with an active oxidation of the silicon present in the substrate at this temperature. Finally, this predominance of alumina at higher temperature may explain why the exponent of the kinetic power-law decreases with temperature and time: n = 0.5 corresponds to the diffusion-controlled growth of silica [43], Naumenko *et al.* [36] have reported lower exponents studying the oxidation of alumina-former alloys. According to these authors, such so-called sub-parabolic kinetics occur when the oxide scale growth is controlled by grain-boundary oxygen diffusion, the diffusion coefficient being related to the inverse of lateral grain size of Al_2O_3. Maruyama *et al.* [21] also observed a preferential diffusion of Al^{3+} and O^{2-} ions through the grain boundaries of the alumina scale, which explained why the oxidation of $Mo(Si_{1-x}Al_x)_2$ is faster than the one of $MoSi_2$ according to their work.

Our SEM observations of the surfaces in figure 9 (d-f) have also shown that the oxide grain size increases with the temperature, with a noticeable preferential oxidation at grain boundaries. Such microstructure evolution during oxidation of KSER has also been observed by Ingemarsson *et al.* [25] who noticed that the alumina scale formed after 72 h at 1373 K in air consists of elongated grains followed by equiaxed grains.

The consequences of the oxidation on the radiative properties are the appearance of interference fringes due to the semi-transparency of the oxide layer and the presences of specific peaks corresponding to the oxide phases. According to the review made by Touloukian and DeWitt [45] and to Brun *et al.* [46], the peaks at 11.5 and 20 µm can be linked to alumina. The pre-oxidized sample presents another peak at 8.9 µm that corresponds to a reflectance drop of silica. This confirms that silica forms during the pre-oxidation at 1373 K, whereas alumina is preponderant in the *in-situ* grown oxide layer.

Finally, these first results are promising for the solar receiver applications: the oxide layer is only 3.3 µm thick after 700 h exposure at 1373 K, which would correspond to approximately three months of use. Moreover, the solar absorptivity α of the surface is slightly higher at 1370 K for the pre-oxidized than for the as-received sample (0.76 vs. 0.71) due to an increase of the spectral emissivity in the 1.4-2.8 µm wavelength range with the presence of interference fringes. Consequently, even if the total emissivity ε of the pre-oxidized sample is also higher than the one of the as-received one (0.65 vs. 0.61) due to the fact the spectral emissivity also increases in the infra-red due to the emissivity peaks of the oxides, the ratio α/ε stays really close (1.16 vs. 1.17). So the oxidation at 1370 K does not degrade significantly the radiative properties of the surface and therefore we can expect that the efficiency of the conversion of the solar concentrated flux into heat will not be affected by the growth of an oxide layer.

5. Conclusion

Oxidation of KSER in air leads to the formation of two oxide phases:

- Alumina forms whatever the oxidation conditions are,
- Silica forms during passive oxidation of the silicon at temperatures up to 1600 K. At temperatures beyond 1850 K, this compound is less present as active oxidation of the silicon in gaseous SiO occurs instead.

The samples oxidized inside the muffle furnace at 1373 K and in the solar furnace at 1600 K follow a semi-parabolic oxidation kinetics, which is coherent with the formation of silica phases, whereas the samples oxidized at 1850 and 2100 K follow a sub-parabolic oxidation kinetics as some alumina-former alloys do.

The formation of alumina during the high temperature radiative measurement on the as-received sample is also visible through the growth of the emissivity peaks at 11.5 and 20 µm.

Another peak at 8.9 µm is present on the pre-oxidized sample that can be linked to the presence of silica phases.

Based on these results, KSER seems a promising alloy for the solar receiver application. After 700 h exposure at 1373 K, the oxide layer is only 3.3 µm thick. Moreover, the presence of this oxide layer does not degrade significantly the radiative properties. Nevertheless, the oxidation is accelerated beyond 1600 K, showing that the material would be more damaged by accidental exposure to a too important solar concentrated flux. The mechanical performance (and the creep or fatigue resistance), the machinability, and the high-temperature thermal properties of KSER have also to be investigated before envisaging this material as a solution for bulk solar receivers. If those performances were not satisfactory, a long-term alternative would be to develop Mo-Al-Si coatings on TZM alloy in order to keep an oxidation resistant layer on a bulk material with convenient mechanical and thermal properties.

CRediT authorship contribution statement
Johan Colas: Conceptualization, Methodology, Solar experimentation, Writing - original draft. **Ludovic Charpentier**: Methodology, Solar experimentation, Writing - review & editing, Funding acquisition, Supervision, Project administration. **Danying Chen**: Conceptualization, Oxidation experimentation, Kinetics analysis, Writing. **Eric Bêche**: XPS measurement, XRD characterization, Writing. **Jérôme Esvan**: XPS measurement, Writing. **Domingos de Sousa Meneses**: Emissivity experimentation, Writing & review. **Frédéric Mercier**: Writing, Supervision. **Michel Pons**: Writing, Supervision. **Marianne Balat-Pichelin**: Methodology, Writing - review & editing, Supervision.

Declaration of interests
The authors declare that they have no known competing financial interests or personal relationships that could have appeared to influence the work reported in this paper.

6. Acknowledgments

This work was supported by the French "Investments for the future" program funded by the French National Research Agency (ANR) under contracts ANR-10-LABX-22-01-SOLSTICE and ANR-10-EQPX-49-SOCRATE, and by the 2MAC-CSP project also funded by the ANR under contract ANR-16-CE08-0019. We also thank Y. Gorand from the University of Perpignan Via Domitia (UPVD) for his help on SEM imaging.

This project would not have been possible without the scientific expertise and human devotion of our co-worker Michel Pons, who passed away recently. We dedicate him this work he was actively involved in, in the memory of the successful meetings we had.

7. Data availability

The raw data required to reproduce these findings cannot be shared at this time due to technical or time limitations. The processed data required to reproduce these findings cannot be shared at this time due to technical or time limitations.

8. References

[1] A. Segal, M. Epstein, Optimized working temperatures of a solar central receiver, Sol. Energy 75 (2003) 503-510. https://doi.org/10.1016/j.solener.2003.08.036

[2] A. Kribus, R. Zaibel, D. Carey, A. Segal, J. Karni, A solar-driven combined cycle power plant, Sol. Energy 62 (1998) 121-129. https://doi.org/10.1016/S0038-092X(97)00107-2

[3] B. Grange, C. Dalet, Q. Falcoz, F. Siros, A. Ferrière, Simulation of a hybrid solar gas-turbine cycle with storage integration, Enrgy Proced. 49 (2014) 1147-1156. https://doi.org/10.1016/j.egypro.2014.03.124

[4] HAYNES® 230® alloy. Haynes International. http://haynesintl.com/docs/default-source/pdfs/new-alloy-brochures/high-temperature-alloys/brochures/230-brochure.pdf?sfvrsn=ae7229d4_80 (last access on October 13th, 2020)

[5] INCONEL® alloy 625. Special Metals Corporation; 2013. https://www.specialmetals.com/assets/smc/documents/alloys/inconel/inconel-alloy-625.pdf (last access on October 13th, 2020)

[6] INCONEL® alloy 718. Special Metals Corporation; 2007. https://www.specialmetals.com/assets/smc/documents/alloys/inconel/inconel-alloy-718.pdf (last access on October 13th, 2020)

[7] B. Jönsson, Q. Lu, D. Chandrasekaran, R. Berglund, F. Rave. Oxidation and Creep Limited
Lifetime of Kanthal APMT®, a Dispersion Strengthened FeCrAlMo Alloy Designed for Strength and Oxidation Resistance at High Temperatures. Oxid Met. 79 (2013) 29‑39. https://doi.org/10.1007/s11085-012-9324-4

[8] R.C. Lobb, R.B. Jones. Creep-rupture properties of fecralloy stainless steel between 650 and 800 °C. J. Nucl. Mater. 91 (1980) 257‑264. https://doi.org/10.1016/0022-3115(80)90225-1

[9] T.E. Tietz, J.W. Wilson. Mechanical, Oxidation, and Thermal Property Data for Seven Refractory Metals and their Alloys. Lockheed Aircraft Corp.; 1961. Report No.: LMSC-6-75-65-22. http://www.dtic.mil/dtic/tr/fulltext/u2/266824.pdf (last access on October 13th, 2020)

[10] D.G. Morris, D.R. Harries. Creep and rupture in Type 316 stainless steel at temperatures between 525 and 900°C Part I: Creep rate. Met. Sci. 12 (1978) 525‑531. https://doi.org/10.1179/msc.1978.12.11.525

[11] M. Radovic, M.W. Barsoum, T. El-Raghy, S.M. Wiederhorn. Tensile creep of coarse-grained Ti_3SiC_2 in the 1000–1200°C temperature range. J. Alloys Compd. 361 (2003) 299‑312. https://doi.org/10.1016/S0925-8388(03)00435-3

[12] J.D. French, S.M. Wiederhorn, J.J. Petrovic. Creep Rupture of $MoSi_2/SiC_p$ Composites. MRS Proc. 322 (1993) 203. https://doi.org/10.1557/PROC-322-203.

[13] G.S. Corman, K.L. Luthra. Silicon Melt Infiltrated Ceramic Composites (HiPerCompTM). In: Bansal NP, éditeur. Handbook of Ceramic Composites. Springer US; 2005. p. 99‑115. https://doi.org/10.1007/0-387-23986-3_5

[14] HAYNES® 214® alloy. Haynes International; 2017. http://haynesintl.com/docs/default-source/pdfs/new-alloy-brochures/high-temperature-alloys/brochures/214-brochure.pdf?sfvrsn=10 (last access on October 13th, 2020)

[15] Kanthal®. http://www.kanthal.com/en/products/material-datasheets/ (last access on October 13th, 2020)

[16] S. Bose, R.J. Hecht. Thermal properties of MoSi2 and SiC whisker-reinforced MoSi2. J. Mater. Sci. 27 (1992) 2749‑2752. https://doi.org/10.1007/BF00540701

[17] Y.S. Touloukian, R.W. Powell, C.Y. Ho, P.G. Klemens. Thermal conductivity - metallic elements and alloys. Vol. 1. IFI/Plenum; 1970.

[18] Plansee. https://www.plansee.com/fr/index.html (last access on October 13th, 2020).

[19] M.W. Barsoum, T. El-Raghy, C.J. Rawn, W.D. Porter, H. Wang, E.A. Payzant, et al. Thermal properties of Ti_3SiC_2. J. Phys. Chem. Solids 60 (1999) 429‑439. https://doi.org/10.1016/S0022-3697(98)00313-8

[20] W. Kowbel, C.A. Bruce, K.L. Tsou, K. Patel, J.C. Withers, G.E. Youngblood. High thermal conductivity SiC/SiC composites for fusion applications. J. Nucl. Mater. 283-287 (2000) 570‑573. https://doi.org/10.1016/S0022-3115(00)00213-0

[21] T. Maruyama, K. Yanagihara, K. Nagata, High temperature oxidation of intermetallic compounds of $Mo(Si_{1-x}Al_x)_2$, Corros. Sci. 35 (1993) 939-944. https://doi.org/10.1016/0010-938X(93)90312-5

[22] L. Ingemarsson, M. Halvarsson, J. Engkvist, T. Jonsson, K. Hellström,L.G. Johansson, J.E. Svensson, Oxidation behavior of a Mo $(Si, Al)_2$-based composite at 300–1000 °C, Intermetallics 18 (2010) 633–640. https://doi.org/10.1016/j.intermet.2009.10.019

[23] L. Ingemarsson, K. Hellström, L.G. Johansson, J.E. Svensson, M. Halvarsson, Oxidation behaviour of a $Mo(Si,Al)_2$ based composite at 1500 °C, Intermetallics 19 (2011) 1319-1329. https://doi.org/10.1016/j.intermet.2011.05.002

[24] J. Colas, L. Charpentier, M. Balat-Pichelin, Oxidation in air at 1400 K and optical properties of Inconel 625, FeCrAlloy and Kanthal Super ER, Oxid. Met. 93 (2020) 355–370. https://doi.org/10.1007/s11085-020-09959-6

[25] L. Ingemarsson, K. Hellström, S. Canovic, T. Jonsson, M. Halvarsson, L.-G. Johansson, J.-E. Svensson, Oxidation behavior of a $Mo(Si,Al)_2$ composite at 900–1600 °C in dry air, J. Mater. Sci. 48 (2013) 1511–1523. https://doi.org/10.1007/s10853-012-6906-0

[26] J.H. Scofield, Hartree-Slater subshell photoionization cross-sections at 1254 and 1487 eV, J. Electron. Spectrosc. 8 (1976) 129-137. https://doi.org/10.1016/0368-2048(76)80015-1

[27] M.P. Seah, in: Practical Surface Analysis (2nd edn), vol. 1, D. Briggs and M.P. Seah (Eds), J. Wiley & Sons, NY, 1993.

[28] D.A. Shirley, High-Resolution X-Ray Photoemission Spectrum of the Valence Bands of Gold, Phys. Rew. B. 5 (1972) 4709-4714. https://doi.org/10.1103/PhysRevB.5.4709

[29] A. Moustaghfir, E. Tomasella, M. Jacquet,.A. Rivaton, B. Mailhot, J.L. Gardette, E. Bêche, ZnO/Al_2O_3 coatings for the photoprotection of polycarbonate, Thin solid films, 515 (2006) 662-665. https://doi.org/10.1016/j.tsf.2005.12.234

[30] L. Charpentier, M. Balat-Pichelin, F. Audubert, High temperature oxidation of SiC under helium with low-pressure oxygen. Part 1: Sintered α-SiC, J. Eur. Ceram. Soc. 30 (2010) 2653-2660. https://doi.org/10.1016/j.jeurceramsoc.2010.04.025

[31] L. Charpentier, M. Balat-Pichelin, D. Sciti, L. Silvestroni, High temperature oxidation of Zr- and Hf- carbides: influence of matrix and sintering additive, J. Eur. Ceram. Soc. 33 (2013) 2867-2878. https://doi.org/10.1016/j.jeurceramsoc.2013.05.022

[32] D. De Sousa Meneses, P. Melin, L. del Campo, L. Cosson, P. Echegut, Apparatus for measuring the emittance of materials from far infrared to visible wavelengths in extreme conditions of temperature, Infrared Phys. Technol. 69 (2015) 96‑101. https://doi.org/10.1016/j.infrared.2015.01.011

[33] D. De Sousa Meneses, P. Melin, L. del Campo, O. Rozenbaum, L. Cosson, Probing high temperature thermal emissive properties of energy materials and coatings with emission spectroscopy augmented by in situ reflection, Infrared Phys. Technol. 108 (2020) 103329 (9 pp.). https://doi.org/10.1016/j.infrared.2020.103329

[34] Reference Solar Spectral Irradiance: Air Mass 1.5, American Society for Testing and Materials (ASTM), USA. http://rredc.nrel.gov/solar/spectra/am1.5/ (last access on October 13th, 2020)

[35] M. Samadzadeh, C. Oprea, H. K. Sharif, T. Troczynski, Comparative studies of the oxidation of $MoSi_2$ based materials: High-temperature oxidation (1000–1600° C), Int. J. Refract. Met. H. 69 (2017) 31-39. https://doi.org/10.1016/j.ijrmhm.2017.07.015

[36] D. Naumenko, B. Gleeson, E. Wessel, L. Singheiser, W.J. Quadakkers, Correlation between the microstructure, growth mechanism, and growth kinetics of alumina scales on a FeCrAlY alloy, Metall. Mater. Trans. A 38A (2007) 2974-2983. https://doi.org/10.1007/s11661-007-9342-z

[37] R.J. Hemley, Pressure dependence of Raman spectra of SiO_2 polymorphs: α-quartz, coesite, and stishovite. In: M. H. Manghnani, Y. Syono (Eds.), High Pressure Research in Mineral Physics: A Volume in Honor of Syuniti Akimoto, Vol. 39, Geophysical Monograph Series. Tokyo, Terra Scientific Publishing Company, 1987, pp. 347–359.

[38] A.N. Trukhin, K. Smits, J. Jansons, A. Kuzmin, Luminescence of polymorphous SiO_2, Radiat. Meas. 90 (2016) 6–13. http://doi.org/10.1016/j.radmeas.2015.12.002

[39] A. Misra, H. Bist, M. Navati, R. Thareja, J. Narayan, Thin film of aluminum oxide through pulsed laser deposition: a micro-Raman study, Mater. Sci. Eng. B 79 (2001) 49–54. https://doi.org/10.1016/S0921-5107(00)00554-7

[40] M. Kadleíková, J. Breza, M. Veselý, Raman spectra of synthetic sapphire, Microelectron. J. 32 (2001) 955–958. https://doi.org/10.1016/S0026-2692(01)00087-8

[41] M. Cai, D.D. Allred, A. Reyes-Mena, Raman spectroscopic study of the formation of t-$MoSi_2$ from Mo/Si multilayers, J. Vac. Sci. Technol. A 12 (1994), 1535-1541. https://doi.org/10.1116/1.579351

[42] M. Balat-Pichelin, J.-L. Sans, E. Bêche, L. Charpentier, A. Ferrière, S. Chomette, Sol. Energ. Mat. Sol. C. 227 (2021), 111066 (12 pp.). https://doi.org/10.1016/j.solmat.2021.111066

[43] B. E. Deal, A. S. Grove, General relationship for the thermal oxidation of silicon, J. Appl. Phys. 36 (1965) 3770–3778. https://doi.org/10.1063/1.1713945

[44] B. Pierrat, M. Balat-Pichelin, L. Silvestroni, D. Sciti, High temperature oxidation of ZrC–20% $MoSi_2$ in air for future solar receivers, Sol. Energ. Mat. Sol. C. 95 (2011) 2228-2237. https://doi.org/10.1016/j.solmat.2011.03.028

[45] Y.S. Touloukian, D.P. Dewitt, Thermophysical properties of matter - The TPRC Data Series - Vol. 8. Thermal radiative properties - Nonmetallic Solids, IFI/Plenum, New York-Washington, 1972.

[46] J. F. Brun, L. del Campo, D. De Sousa Meneses, P. Echegut, Infrared optical properties of α-alumina with the approach to melting: γ-like tetrahedral structure and small polaron conduction, J. Appl. Phys. 114 (2013) 223501 (5 pp.). https://doi.org/10.1063/1.4846077

List of figure captions

Figure 1. Figures of merit of various materials envisaged for solar applications: thermal conductivity vs creep stress (a), oxidation maximum temperature in dry air vs creep stress (b), fracture toughness vs oxidation maximum temperature in dry air (c).

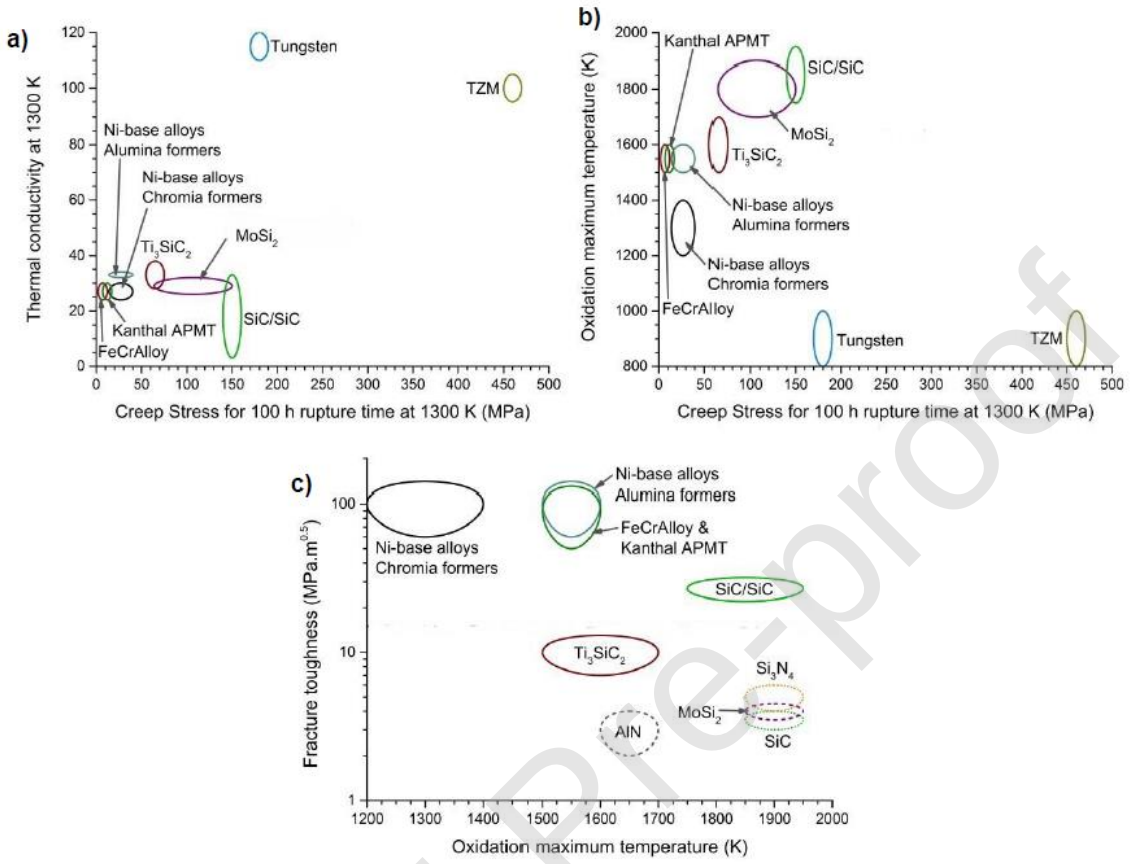

Figure 2. Mass variation with time for four samples oxidized in air inside a muffle furnace at T = 1373 K for 24, 36, 48 and 700 h. (a) Global trend on the full time scale. (b) Zoom on the 0-48 h time interval.

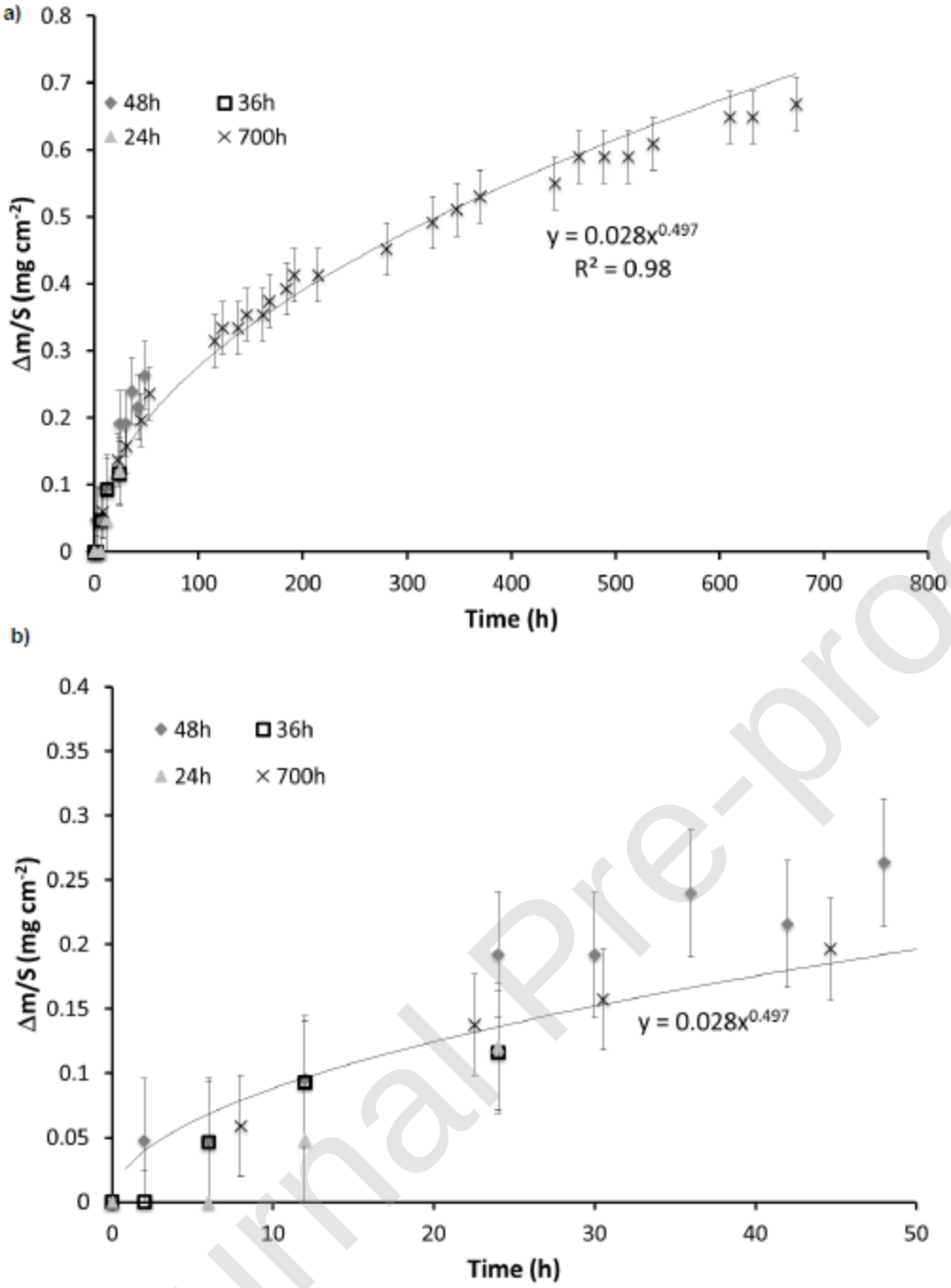

Figure 3. Mass variations of the samples oxidized in air in the REHPTS solar facility at 1600, 1850 and 2100 K.

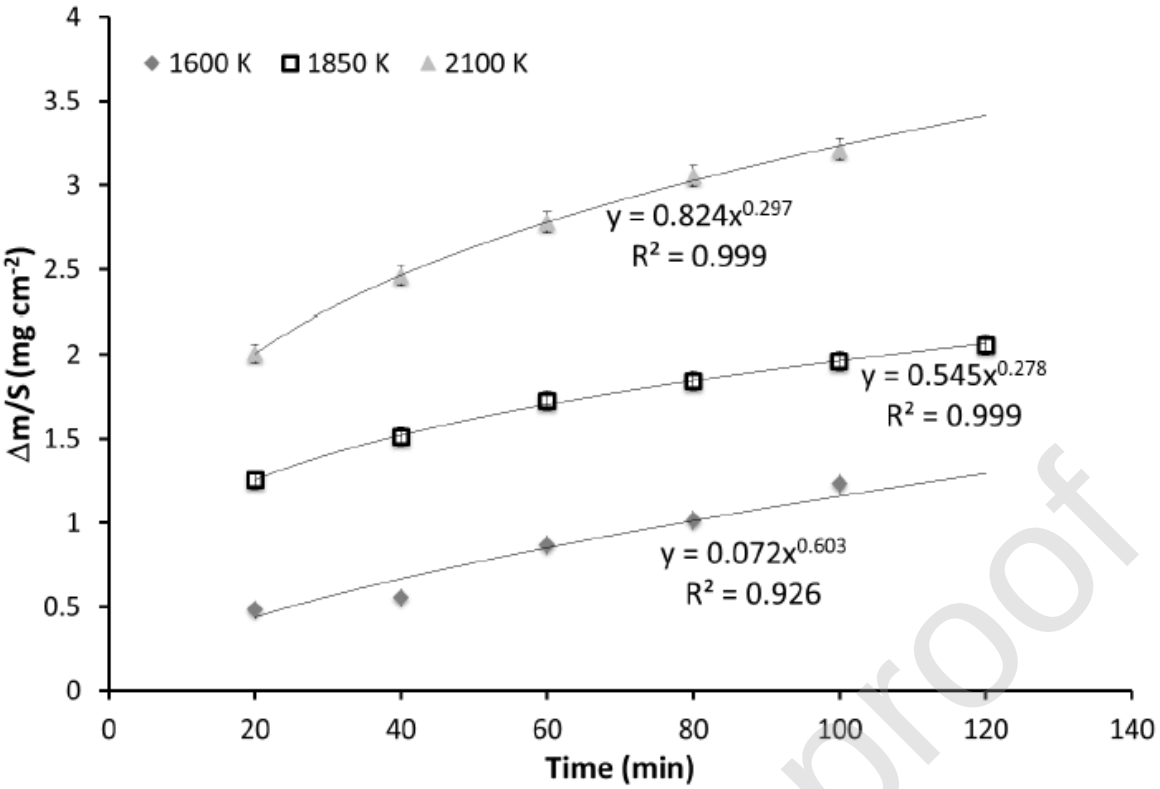

Figure 4. XRD patterns of unoxidized and oxidized KSER in air in (a) muffle furnace at 1373 K and after different time, (b) REHPTS facility at various temperatures and times.

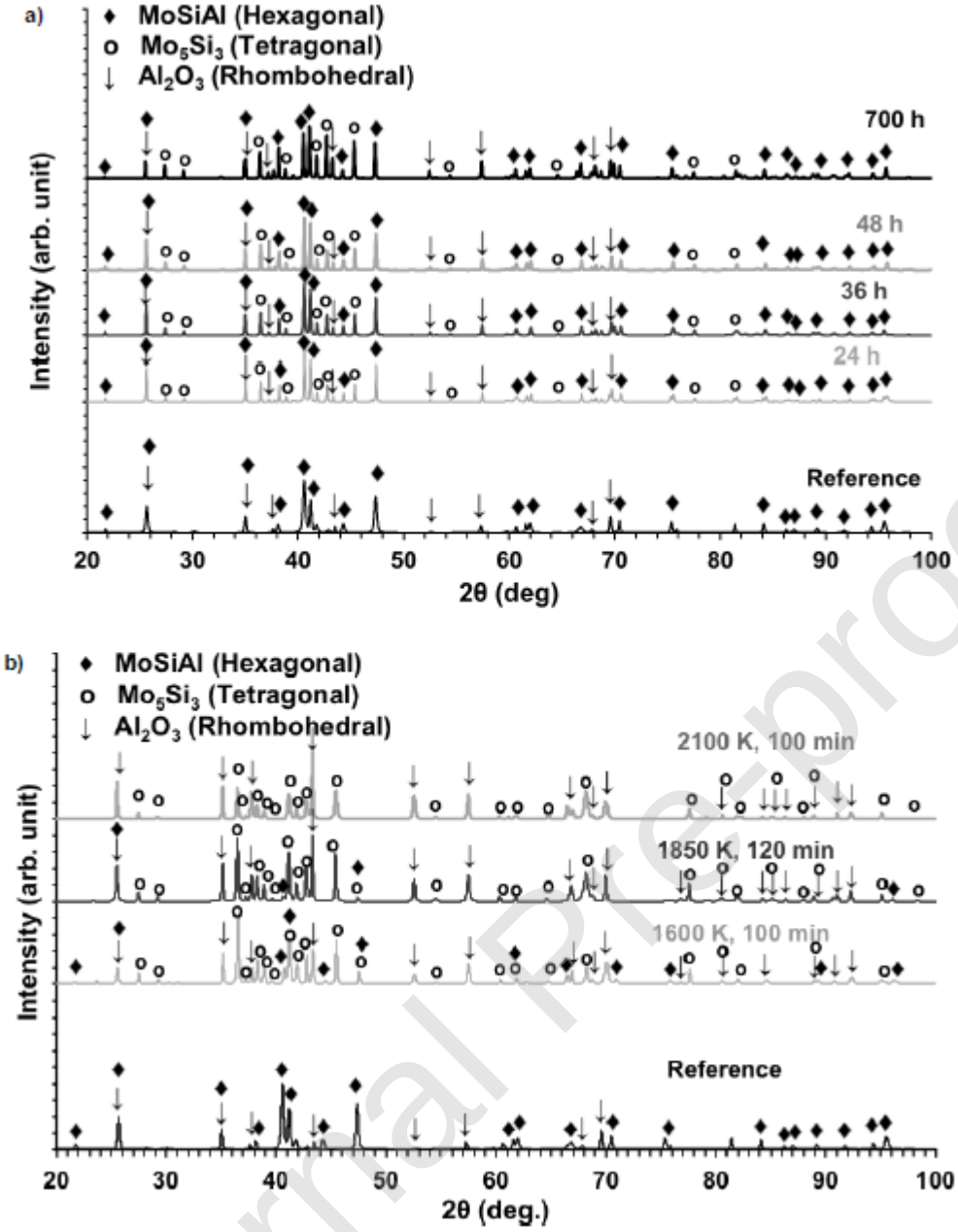

Figure 5. μ-Raman spectra of unoxidized and oxidized KSER in (a) muffle furnace at 1373 K and after different duration times, (b) REHPTS facility at various temperatures and times.

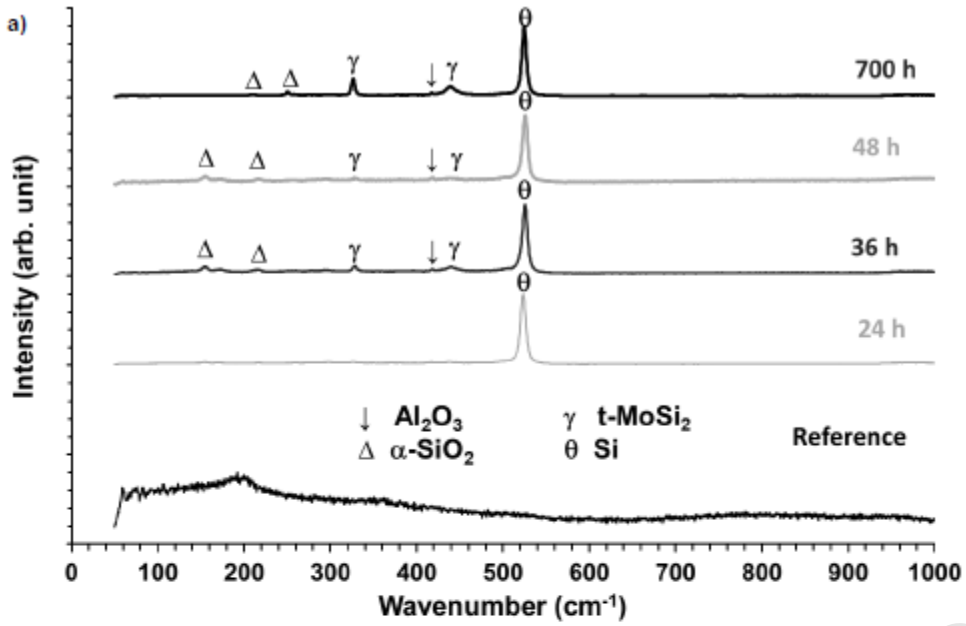

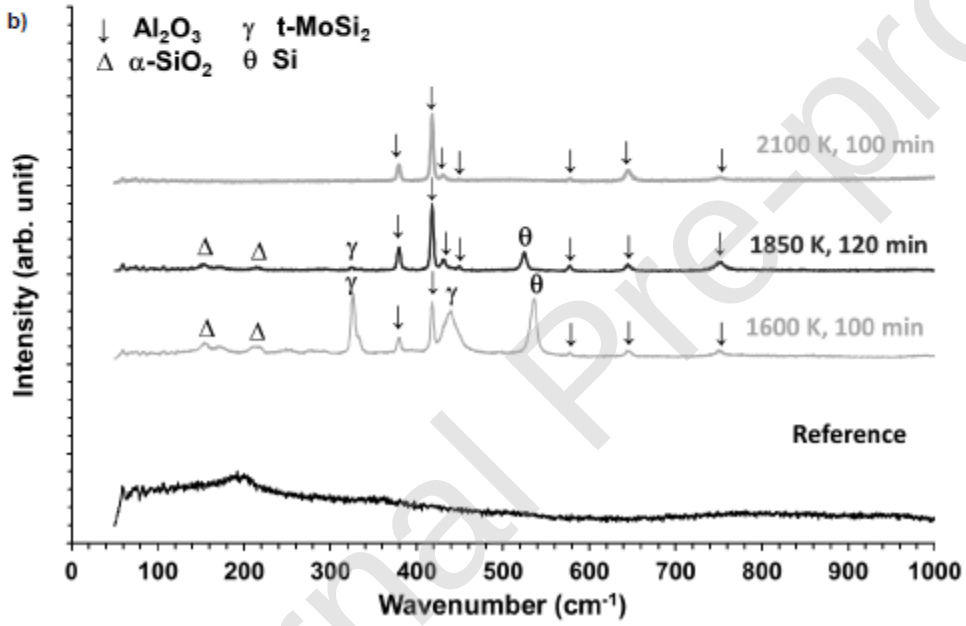

Figure 6. O 1s photoelectron peaks measured on (a) unoxidized KSER sample (b) KSER oxidized during 36 h in air at 1373 K in the muffle furnace and (c) KSER oxidized in air inside REHPTS at 3 different temperatures and during 100 or 120 min.

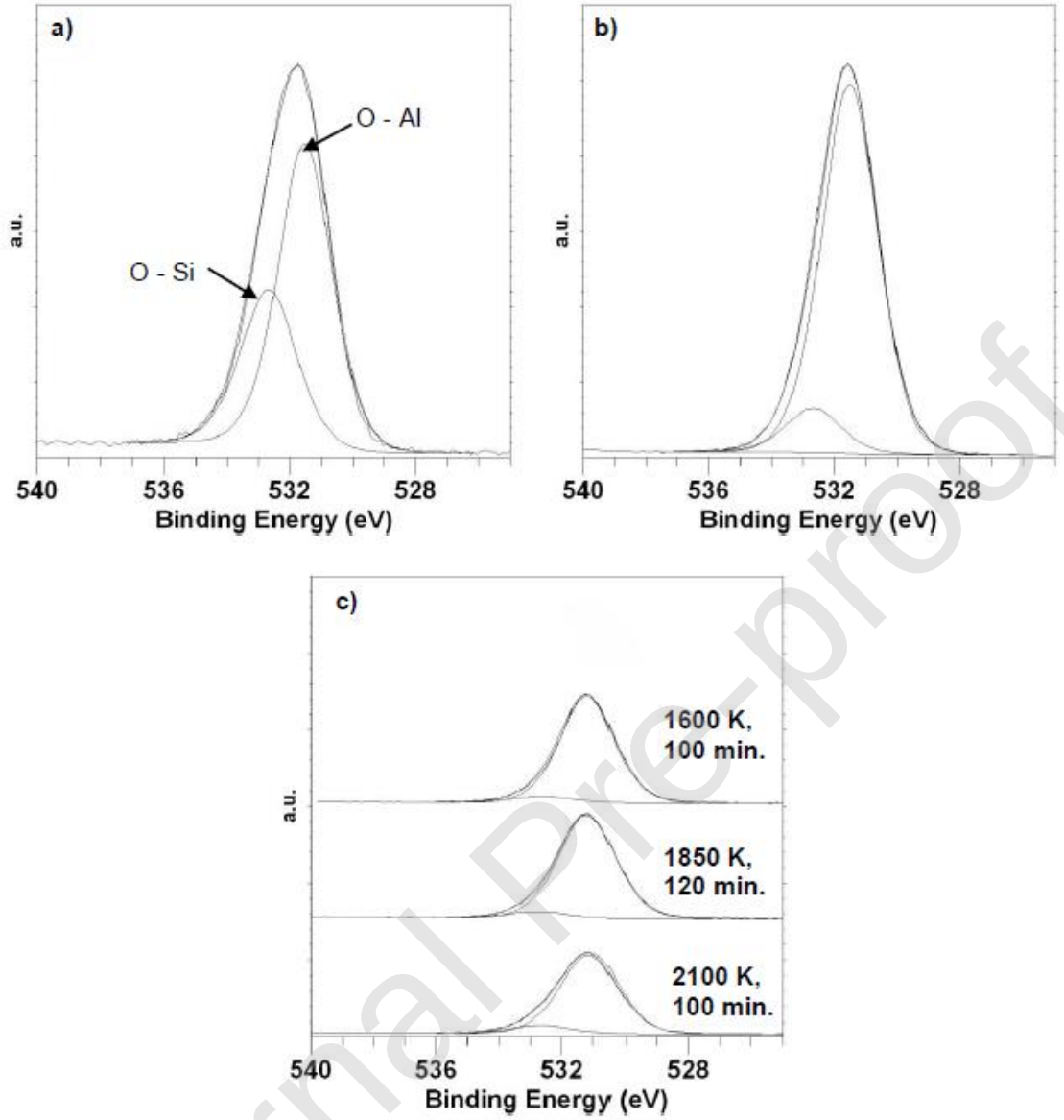

Figure 7. SEM images (SE) of the cross-sections of the samples oxidized in air inside the muffle furnace at 1373 K during (a) 36 h, (b) 48 h and (c) 700 h. The white arrows delimitate the oxide layer.

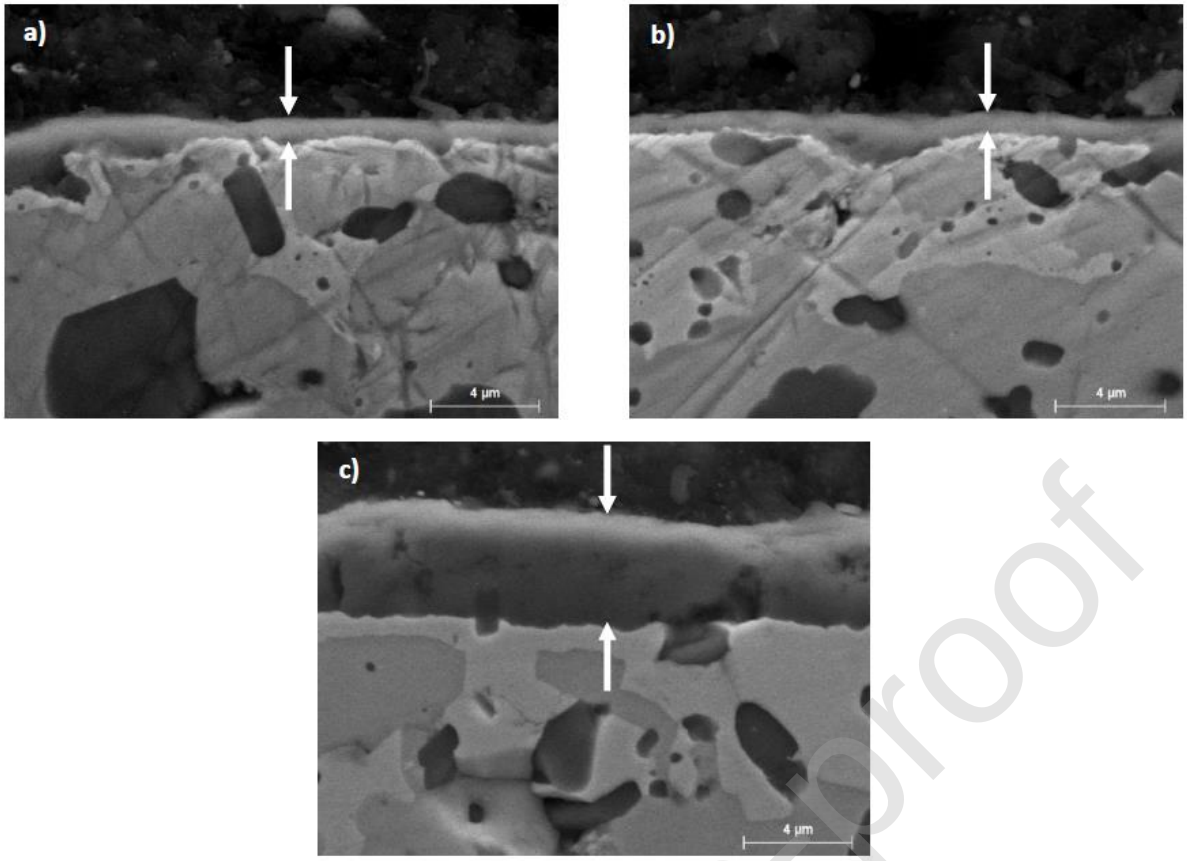

Figure 8. SEM images (SE) of the cross-sections of the samples oxidized in air inside REHPTS facility (a) at T = 1600 K, during 100 min. (b) at T = 1850 K during 120 min. (c) at T = 2100 K during 100 min. The white arrows delimitate the oxide layer. (d-f) EDS spectra corresponding to the area spotted on figure 8 b.

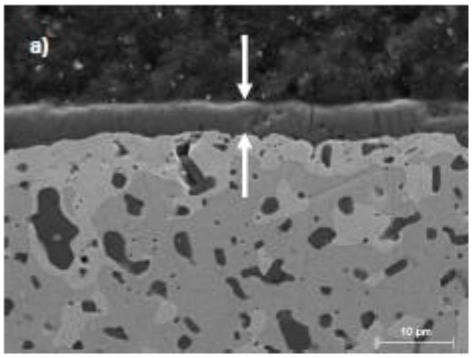

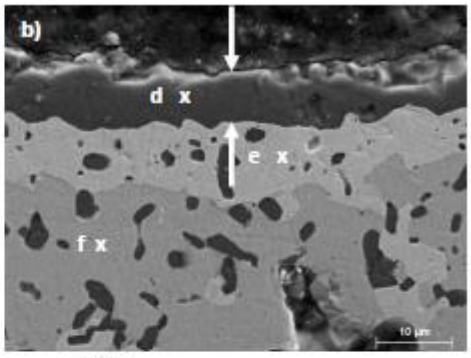

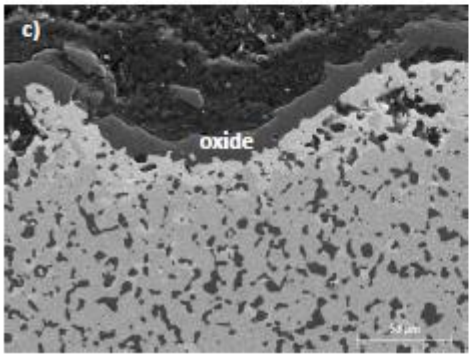

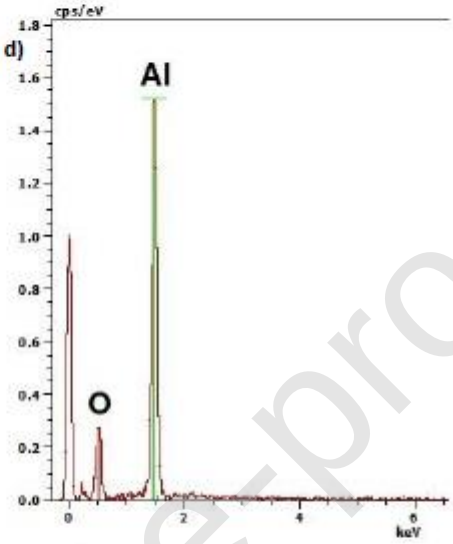

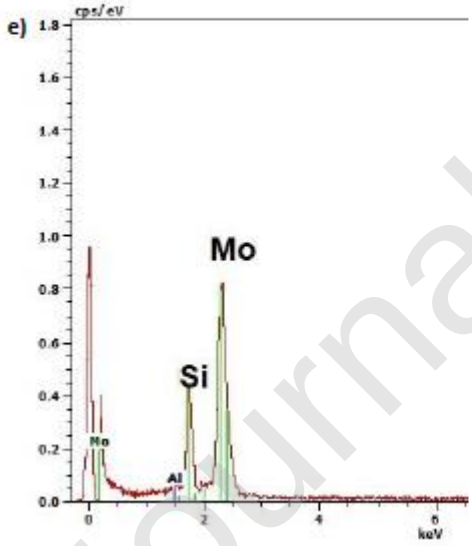

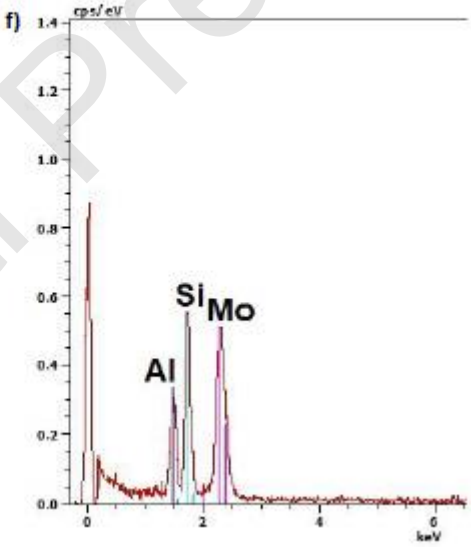

Figure 9. SEM images of the surface of (a) unoxidized KSER and KSER oxidized in air (b-c) inside the muffle furnace at 1373 K during (b) 24 h or (c) 48 h or (d-f) inside REHPTS facility, (d) 100 min. at 1600 K, (e) 120 min. at 1850 K or (f) 100 min. at 2100 K.

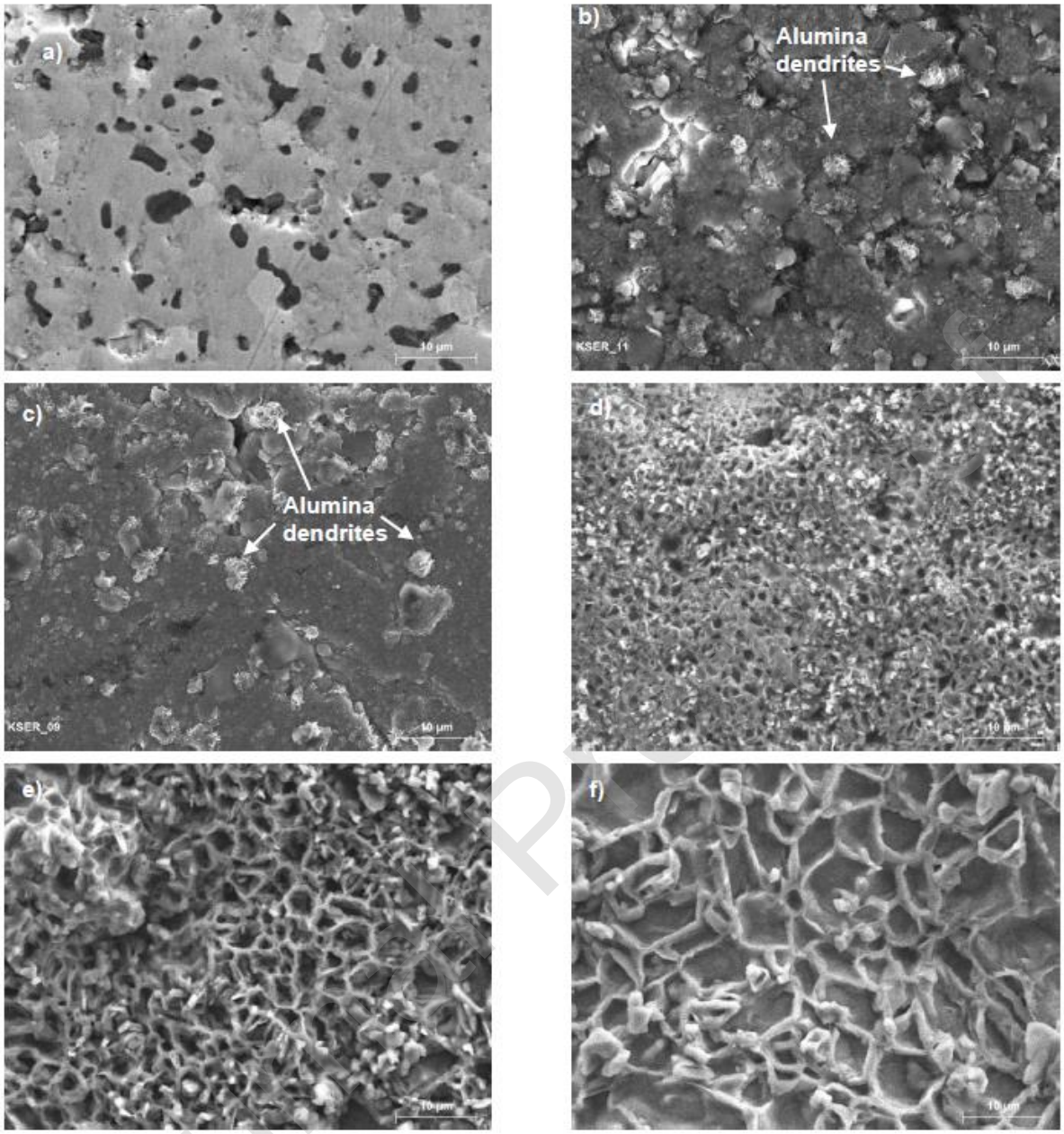

Figure 10. Evolution of the normal spectral emissivity with temperature measured on (a) as-received and (b) pre-oxidized (1373 K in air during 48 h) KSER samples.

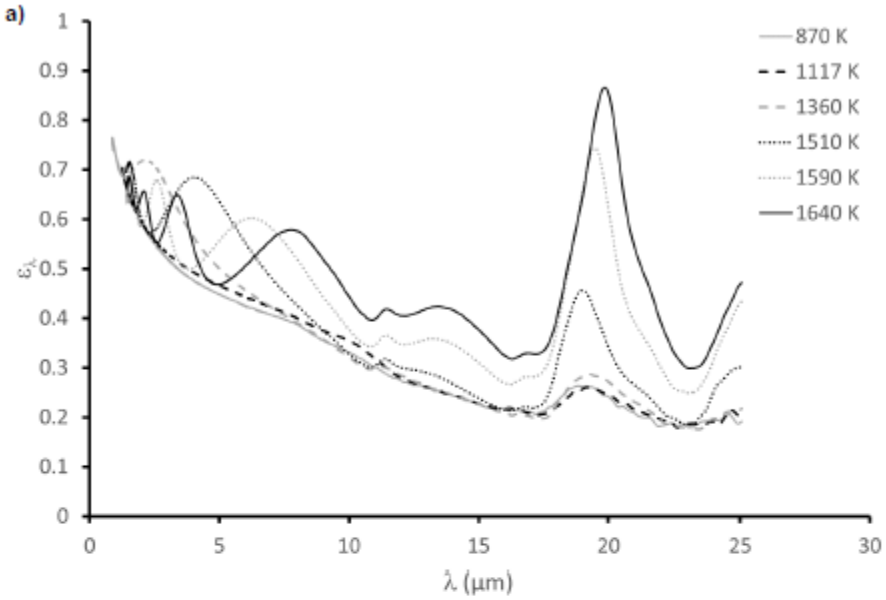

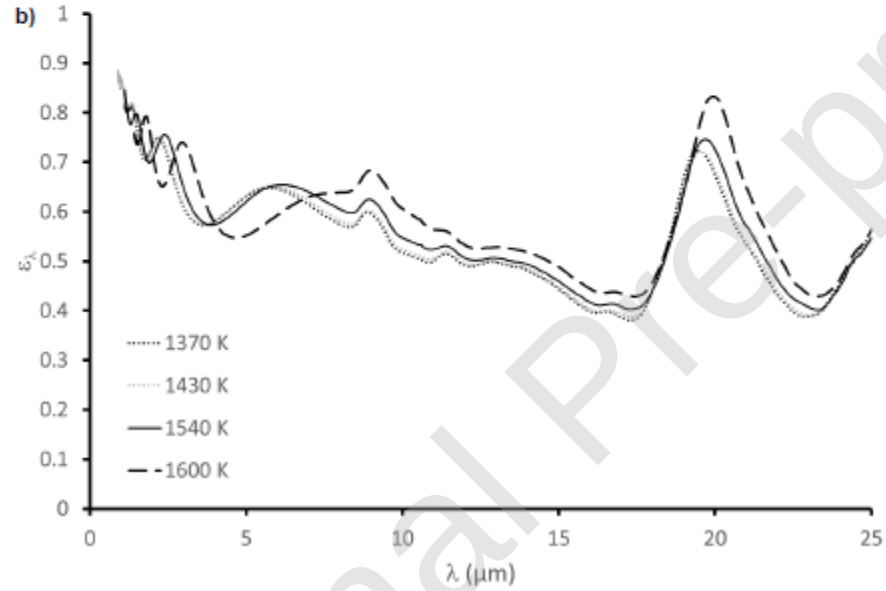

List of table captions

Table 1. Proportion (in atomic %) of the components and of the main chemical bonds (and associated energy) from XPS analyses.

Table 2. Estimated values of the solar absorptivity α, total emissivity ε and α/ε ratio from the high temperature normal spectral emissivity measurements, for as-received and pre-oxidized KSER samples.